Supporting Information:
Modulation of electrostatic interactions to reveal a reaction network unifying the aggregation behaviour of the Aβ42 peptide and its variants.

Georg Meisl, Xiaoting Yang, Christopher M. Dobson, Sara Linse
and Tuomas P. J. Knowles

1 Additional experiments and fits

1.1 Full datasets from Fig. 4

For clarity we showed only part of the dataset in the fits in Fig. 4. The full datasets are shown here in Fig. S1. Note that the fits shown in the main text were also performed on the entire dataset, i.e. they are the same as the ones shown here, some concentrations were simply omitted for clarity.

1.2 Fitting reaction orders

In the main text we noted a slight deviation of the fits in the parallel limit at high monomer concentrations, Fig. 4. This may in fact be due to a small increase in the reaction order of secondary nucleation, e.g. due to an increase in secondary nucleus size. A freely varying n_2 achieved fits to the experimental data within error, as shown in Fig. S2, with a value of $n2 \approx 4$. However, the improvement in the fit is small and all other salt concentrations fit well to a value of $n2 = 2$. In addition a constant value of n_2 across the salt concentration allows for better comparison of the fitted rates. In the main text we therefore chose to keep n_2 fixed to a value of 2.
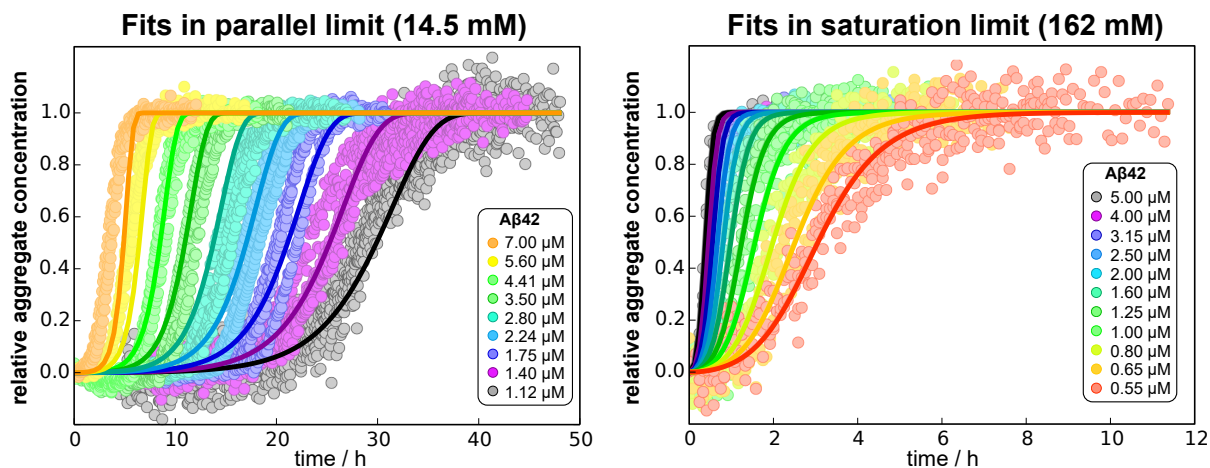
Figure S1: **Fits from Fig. 4.** In Fig. 4 only part of the dataset was shown, here we display all monomer concentrations for the fits in the parallel limit to the data at 2.5 mM salt and the fits in the saturation limit to the data at 150 mM salt.
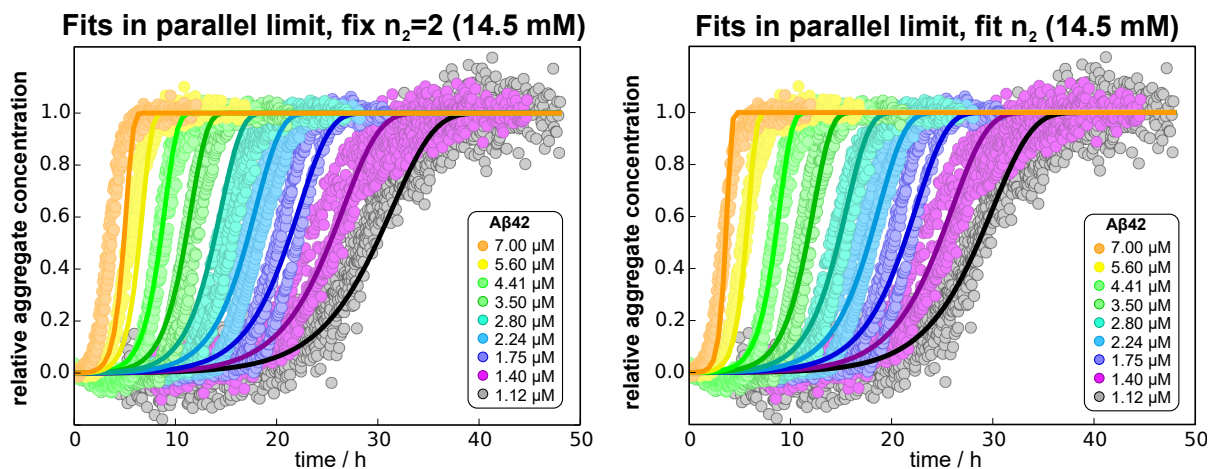

Figure S2: **Fit of the full kinetic curves at 2.5 mM salt with n_2 as a free parameter.** On the left the secondary nucleation reaction order, n_2, is fixed to 2, which is the case used in the main text, on the right n_2 is left to vary during the fitting. n_2 converged to a value of 4, when left to vary, yielding slightly improved fits compared to the case of $n_2 = 2$.

1.3 Detailed variation of rates with salt.

The entire experimental setup was repeated and Fig. S3 shows the scaling exponent obtained from the second set of experiments and is in agreement with the findings of the first set of experiments. In Figs. S4, S5 and S6, the rates from fits of both limits at all salt concentrations are shown. The entire setup was performed twice, labelled set 1 and set 2 in the figures, the results from the two datasets agree well. By considering the saturation of secondary nucleation at high salt we can now explain the discontinuity observed in the parameters obtained from fits in the parallel limit: At high salt concentrations the secondary nucleation process is saturated at all monomer concentrations. In a fully saturated system the term for secondary nucleation has no monomer dependence and becomes $k_2 \frac{m(t)^{n_2}}{1+m(t)^{n_2}/K_M} M(t) \rightarrow k_2 K_M M(t)$ (details see section "Further special cases/limits" below) which is equivalent to a system purely determined by fragmentation, with fragmentation rate constant $k_- = k_2 K_M$. Hence the parallel limit yields good, purely fragmentation dominated fits at high salt concentrations, but the fragmentation rate constant obtained from the fit is in fact the saturated secondary nucleation rate constant, meaning that the discontinuities in k_- and k_2 in the parallel limit results from the fact that we are fitting to actual fragmentation at low salt concentrations and misinterpreting saturated secondary nucleation as fragmentation at high salt concentrations.
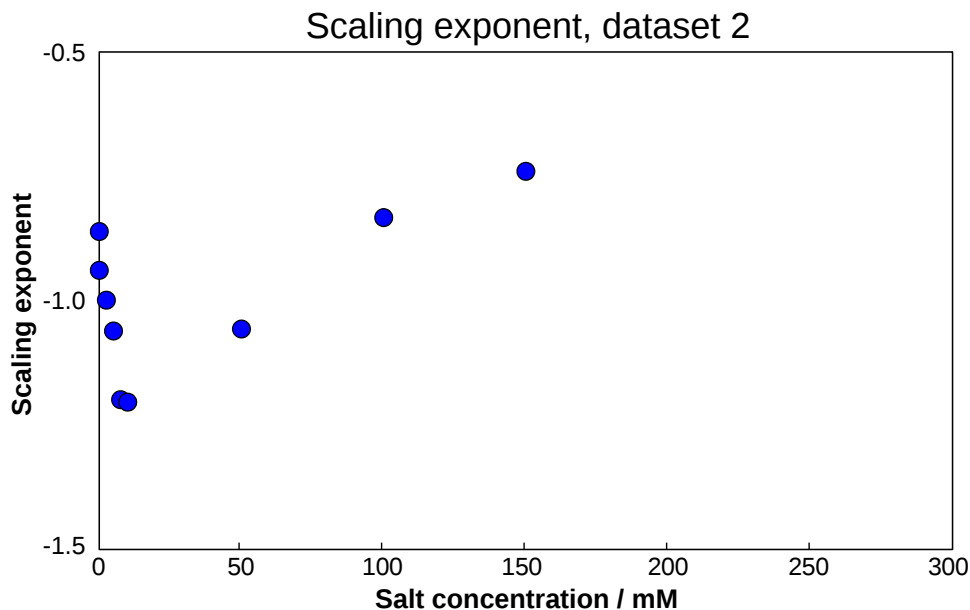

Figure S3: **Variation of the average scaling exponent.** This is equivalent to the plot in Fig. 2c in the main text, for the repeat dataset, and shows very similar results.
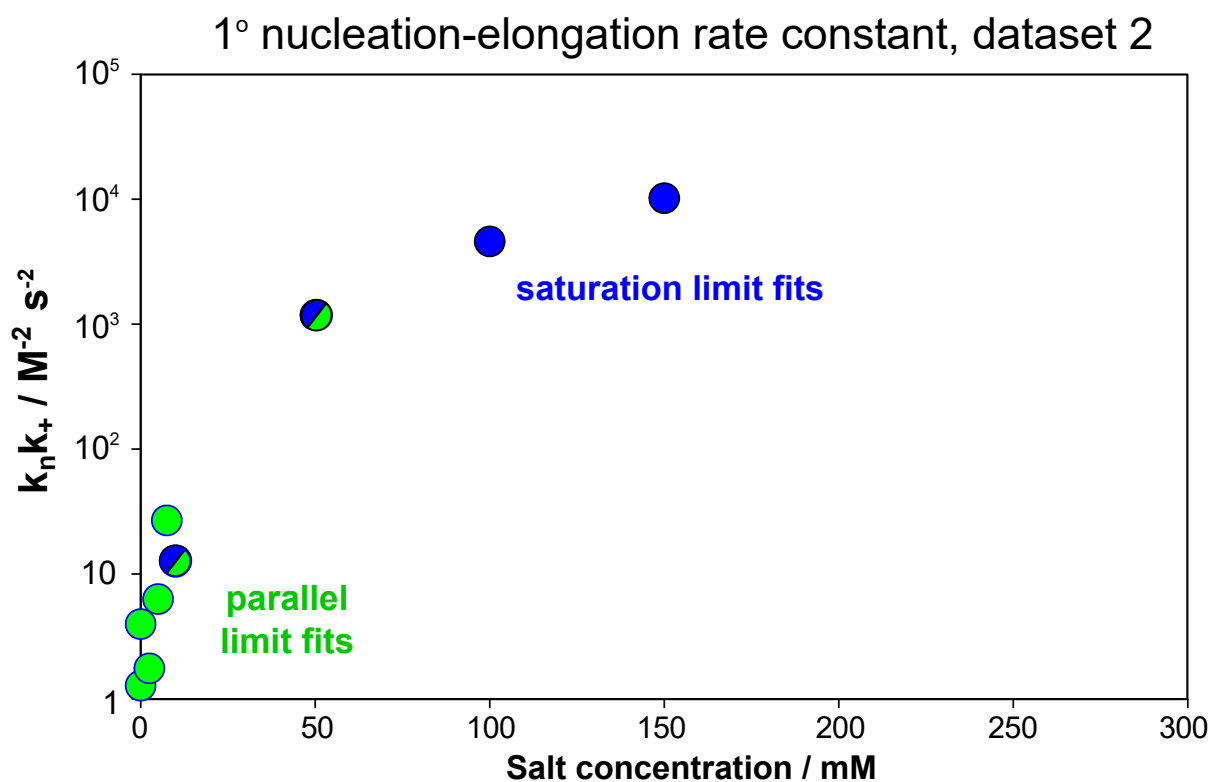
Figure S4: **Variation of the combined primary nucleation-elongation rate constant.** This is the equivalent of Fig. 6b in the main text, for the repeat dataset, and shows very similar results.
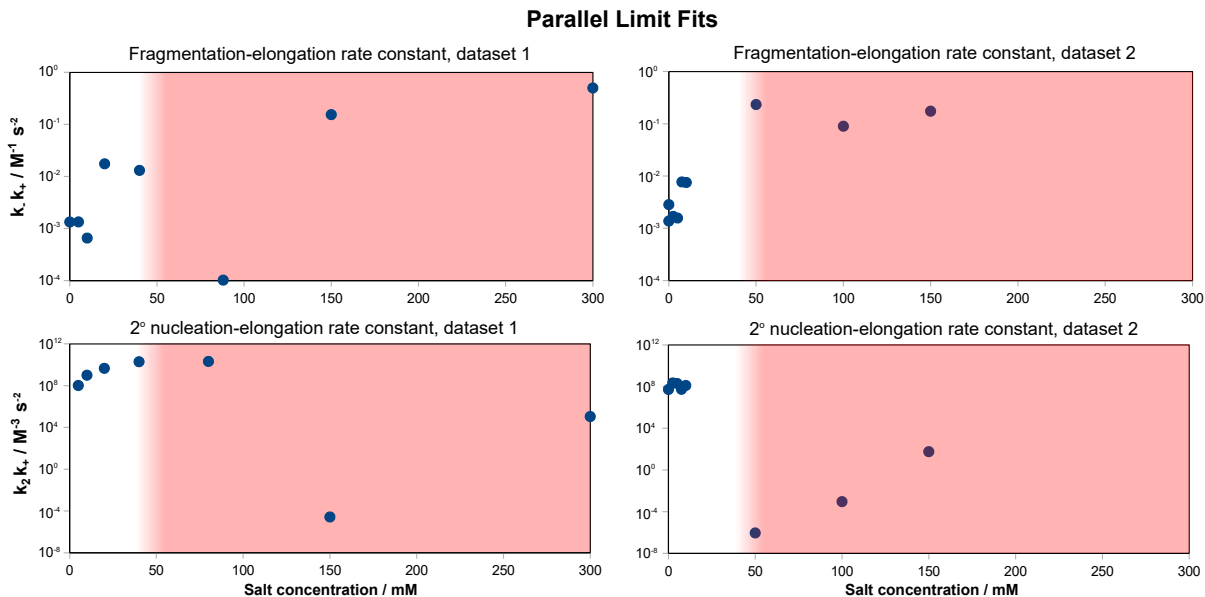
Figure S5: **Variation of the microscopic rates with salt concentration in the parallel limit.** The region in which we found the parallel limit to be no longer valid (above approximately 50 mM salt) is marked in red. The top panels show the combined fragmentation-elongation rate constant. The bottom panels show the combined secondary nucleation - elongation rate. Note the major discontinuity in k_+k_2 (15 orders of magnitude), which marks the point at which the parallel limit is no longer valid, i.e. when saturated secondary nucleation is suddenly interpreted as fragmentation as explained in detail in the text. In the region of validity, k_+k_2 increases by several orders of magnitude, whereas k_+k_- only increases by one order of magnitude. As the elongation rate constant was independently determined to increase by one order of magnitude, the increase in k_+k_- can hence be attributed purely to the increase in elongation. Therefore the fragmentation rate depends only weakly on the salt concentration, whereas the secondary nucleation rate constant (also confirmed by fits in the saturation limit) increases significantly with increasing salt concentration.
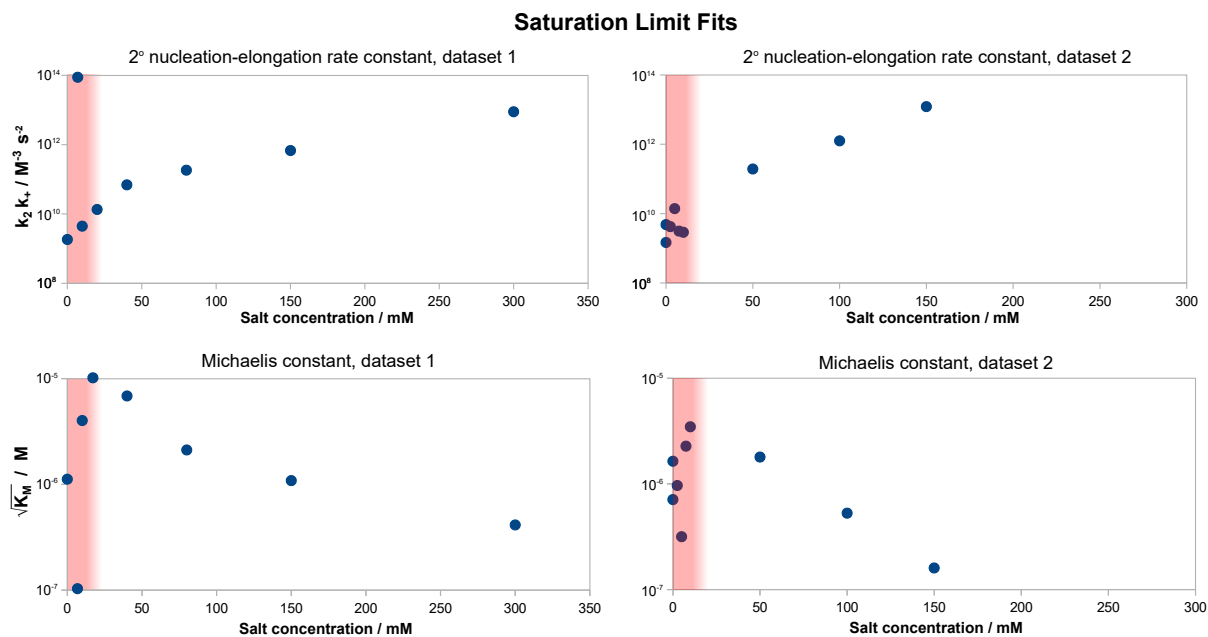
Figure S6: **Variation of the microscopic rates with salt concentration in the saturation limit.** The region in which we found the saturation limit to be no longer valid (below approximately 10 mM salt) is marked in red. The top panels show the combined secondary nucleation-elongation rate constant. The bottom panels show the square root of the Michaelis constant, i.e. the concentration at which saturation effects are most significant. In its region of validity, the secondary nucleation rate constant increase by about 2 orders of magnitude, the elongation rate constant, which was determined independently, shows only a weak increase in this region, hence secondary nucleation is clearly favoured by an increase in salt concentration. The Michaelis constant displays erratic behaviour in the region where the saturation limit is not valid, as these values were obtained from missfits. In its region of validity there is a clear trend going from an unsaturated system, with saturation concentrations above the highest sampled monomer concentrations, to a saturated system, with saturation concentrations below the lowest sampled monomer concentrations.

2 Theoretical Background and Detailed Solutions

2.1 Model derivation

We make two basic assumptions, first that the increase in fibril mass is proportional to the number of fibrils (this is motivated by considering addition to the ends of fibrils only; the area and structure of the ends is not expected to change with fibril length) and that the processes creating new fibrils are proportional to the total fibril mass (what we will call secondary processes; this includes fibril surface catalysed nucleation and fragmentation of fibrils). Using simple chemical kinetics we can then derive differential equations, the moment equations, describing the time evolution of fibril number concentration, $P(t)$, and fibril mass concentration, $M(t)$.

$$\frac{dP}{dt} = k_n m(t)^{n_c} + k_-(M(t) - (2n_c - 1)P[t]) + k_2 \frac{m(t)^{n_2}}{1 + m(t)^{n_2}/K_M} M(t) \quad \text{(S1)}$$

$$\frac{dM}{dt} = 2m(t)k_+ P(t) \quad \text{(S2)}$$

The origin of the terms in equation (S1) from left to right is primary nucleation, fragmentation and secondary nucleation. In previous work [9] it was shown that secondary nucleation may saturate at high monomer concentrations, i.e. become monomer independent. This is reflected in the term $\frac{m(t)^{n_2}}{1+m(t)^{n_2}/K_M}$ which originates from a treatment of secondary nucleation as a Michaelis-Menten like process resulting in saturation kinetics: At low monomer concentrations secondary nucleation depends on monomer to the power of n_2 ($\frac{m(t)^{n_2}}{1+m(t)^{n_2}/K_M} \approx m(t)^{n_2}$), whereas at high monomer concentrations it is independent of monomer concentration ($\frac{m(t)^{n_2}}{1+m(t)^{n_2}/K_M} \approx K_M$). The Michaelis constant K_M determines at which concentration this change of behaviour occurs. For a more detailed discussion of the two limits see section 2.2.

The solution to these equations in the limit $K_M \to \infty$ (parallel limit) is outlined below and in the limit $k_- \to 0$ (saturation limit) it is found in "Differences in nucleation behaviour underlie the contrasting aggregation kinetics of the Aβ40 and Aβ42 peptides" [9].

In the parallel limit the system of differential equations to solve becomes:

$$\frac{dP}{dt} = k_n m(t)^{n_c} + k_- M(t) + k_2 m(t)^{n_2} M(t) \quad \text{(S3)}$$

$$\frac{dM}{dt} = 2m(t)k_+ P(t) \quad \text{(S4)}$$

where we ignored the term $-(2n_c - 1)P[t]$ for clarity. It accounts for the fibrils lost when a piece smaller than the critical nucleus breaks off and dissolves, which is negligible for the small nucleus size at hand. We find the early time solution to these equations by setting $m(t) = m(0)$; this linearises the equations and makes them easily solvable. Then,

by integrating equation S3 we obtain a fixed point operator and substitute the early time solution as an initial guess into this fixed point operator to yield the first order solution for $M(t)$. This follows the strategy outlined in detail in Cohen *et al.*(2011) [5, 4]. The approximate solution obtained in this way is given by:

$$
\begin{aligned}
M(t) &= m_{\text{tot}} + \text{Exp}\left[-\frac{k_+(4c\kappa\text{Cosh}(\kappa t) + 4P_0\kappa^2\text{Sinh}(\kappa t))}{2\kappa^3}\right] \\
&\quad \left((M_0 - m_{\text{tot}})e^{\frac{2k_+c}{\kappa^2}}\right)
\end{aligned}
\tag{S5}
$$

where

$$
\begin{aligned}
a &= k_2 m_0^{n_2} + k_- \\
c &= k_n m_0^{n_c} + aM_0 \\
\kappa &= \sqrt{2k_+ m_0(k_2 m_0^{n_2} + k_-)}
\end{aligned}
\tag{S6}
$$

where m_{tot} is the total protein concentration, M_0, P_0 and m_0 are the initial mass concentration of fibrils, number concentration of fibrils and monomer concentration respectively, k_+, k_-, k_n and k_2 are the rate constants of elongation, fragmentation, primary nucleation and secondary nucleation.

Note that for unseeded experiments the two limiting cases only involve 3 free parameters each ($k_+ k_2$, $k_+ k_n$ and $k_+ k_-$ in the parallel limit and $k_+ k_2$, $k_+ k_n$ and K_M in the saturation limit) which are sufficient to produce good global fits to all monomer concentrations at any given salt concentration.

In the parallel limit the scaling exponents is given by

$$
\gamma_{\text{comp}} = \frac{d\log(t_{1/2})}{d\log(m(0))} \approx -\frac{1}{2}\left(\frac{n_2}{1 + K/m(0)^{n_2}} + 1\right)
\tag{S7}
$$

where $K = k_-/k_2$. This interpolates between $\gamma = -1/2$ and $\gamma = -(n_2 + 1)/2$ for the limits of low and high monomer respectively, giving the negative curvature in the double logarithmic plots of the half time, as predicted from the qualitative argument used to derive the general constraints above.

In the saturation limit the scaling exponent is given by

$$
\gamma_{\text{sat}} \approx -\frac{1}{2}\left(\frac{n_2}{1 + m(0)^{n_2}/K_M} + 1\right)
\tag{S8}
$$

where K_M is the Michaelis constant. This interpolates between $\gamma = -(n_2 + 1)/2$ and $\gamma = -1/2$ for the limits of low and high monomer respectively, i.e. the reverse of the other limit.

2.2 Further special cases/limits

A fully saturated system in the saturation limit $(m(t)^{n_2} \gg K_M)$ is mathematically equivalent to, but physically distinct from, a purely fragmentation dominated system in the parallel limit $(k_- \gg k_2 m(t)^{n_2})$ as they both include a single, monomer-independent secondary process. This explains why reasonable fits in the parallel limit were achieved at high salt concentrations, albeit with a discontinuity in the fitted rates compared to lower salt, because saturated secondary nucleation was misinterpreted as fragmentation by the fitting, leading to unrealistic behaviours of the associated rates.

Equally, a completely unsaturated system in the saturation limit $(m(t)^{n_2} \ll K_M)$ is mathematically and physically equivalent to a purely secondary nucleation dominated system in the parallel limit $(k_- \ll k_2 m(t)^{n_2})$ as they both include one single-step, monomer-dependent secondary process. However, because the analytical solutions given above are approximate, they do in fact not converge to exactly the same solutions in these limits. The solution in the parallel limit is obtained through one fixed point iteration of the early time linearised solutions, whereas the solution in the saturation limit is obtained from one fixed point iteration of a slightly improved initial guess [5, 4, 9], meaning that the analytical solutions in the saturation case are more accurate, although this effect is minor under most conditions. This may be one of the reasons the fits in the region where both limits are valid do not agree perfectly.

2.3 A note on oligomers

Oligomeric species are thought to play an important role in connection with disease, hence we briefly outline how they fit into the models presented here. Within the definitions of these models, fibrils are species that elongate with a length-independent rate constant and show little dissociation. Therefore, the formation of non-fibrillar oligomers would be subsumed into the nucleation step in our models. That is, the nucleation steps can be a coarse-graining of a multi-step process including intermediate oligomers into a single nucleation step. Under the conditions used in this work, there is no significant build-up of oligomeric species and we find that our coarse-grained description is sufficient to reproduce the kinetics. However, if more detailed data, for example including a direct measurement of the number of small species, is to be analysed, a more detailed modelling of the nucleation steps may be required. Nucleation cascades, which would describe the formation of these species, are discussed in connection with our models in Garcia et al.[7]

2.4 Surface plasmon resonance (SPR) data analysis

The SPR experiments measure the variation of surface bound mass. The experiment consists of two parts. Initially a solution containing monomer is flown past the bound fibrils, during this phase the mass increases due to elongation of surface-bound fibrils and due to adsorption of monomers onto the surface of the bound fibrils. Then, pure

buffer, not containing any monomer, is flown past the surface and the mass decreases, due to loss of the surface bound species and due to detachment from the fibril ends. We treat the elongation process and surface adsorption processes separately, i.e. we assume that the increase in fibril mass due to elongation does not affect the surface adsorption. The elongation reaction is described by the differential equation:

$$\frac{dM}{dt} = (k_+ m_0 - k_{\text{off}}) P_0 \tag{S9}$$

where the fibril number, P_0, and the monomer concentration, m_0, remain constant and k_{off} is the dissociation rate from the fibril ends. Solving this equation yields:

$$M(t) = M_0 + (k_+ m_0 - k_{\text{off}}) P_0 t \tag{S10}$$

The adsorption to the surface can be described simply by:

$$\frac{dm_b}{dt} = k_a m_0 (\alpha M_0 - m_b(t)) - k_d m_b(t) \tag{S11}$$

where k_a and k_d are the rate constants of adsorption and detachment respectively, m_b is the mass bound and α is the number of binding sites on the fibril surface per monomer in the fibril. The solution to this equation is given by:

$$m_b(t) = \frac{e^{-(k_d + k_a m_0)t}(k_d m_{b,0} + k_a m_0 m_{b,0} - k_a m_0 M_0 \alpha + e^{(k_d + k_a m_0)t} k_a m_0 M_0 \alpha)}{k_d + k_a m_0} \tag{S12}$$

where $m_{b,0}$ is the initial concentration of bound monomer.

In the desorption part of the experiment (when only buffer is flown past, so $m_0 = 0$), these equations simplify considerably to give the overall absorbed mass as a sum of $m_b(t)$ and $M(t)$:

$$M_{\text{abs}}(t) = M_0 - k_{\text{off}} P_0 t + m_{b,0} e^{-k_d t} \tag{S13}$$

We fitted equation S13 to the desorption part of the experimental data, to obtain the detachment rate, k_d, as well as the coverage at the beginning of the desorption, $m_{b,0}$, and the coefficient of the linear term, $k_{\text{off}} P_0$ (see Fig. S7). Note that $m_{b,0}$ and P_0 are not expected to be the same for repeats of the same experiment as a different number of fibrils may be bound to the surface.

In the adsorption part of the experiment (when the monomer in solution is at a constant concentration of m_0 and at time 0 there is no monomer bound, $m_{b,0} = 0$), equation S12 simplifies to give the overall absorbed mass as a sum of $m_b(t)$ and $M(t)$:

$$M_{abs}(t) = M_0 + (k_+ m_0 - k_{\text{off}}) P(t) + \frac{(1 - e^{-(k_d + k_a m_0)t}) k_a m_0 M_0 \alpha}{k_d + k_a m_0} \tag{S14}$$

Using the values obtained for k_d, $m_{b,0}$ and $k_{\text{off}} P_0$ in the fits of the decrease of the corresponding experiment, we fitted the increasing portion to equation S14 (see Fig. S7).

For each experiment the ratio k_d/k_a was determined, giving an estimate of the dissociation constant K_D. The four values of K_D obtained at each ionic strength were averaged to yield the mean and standard errors shown in Fig. 6c.
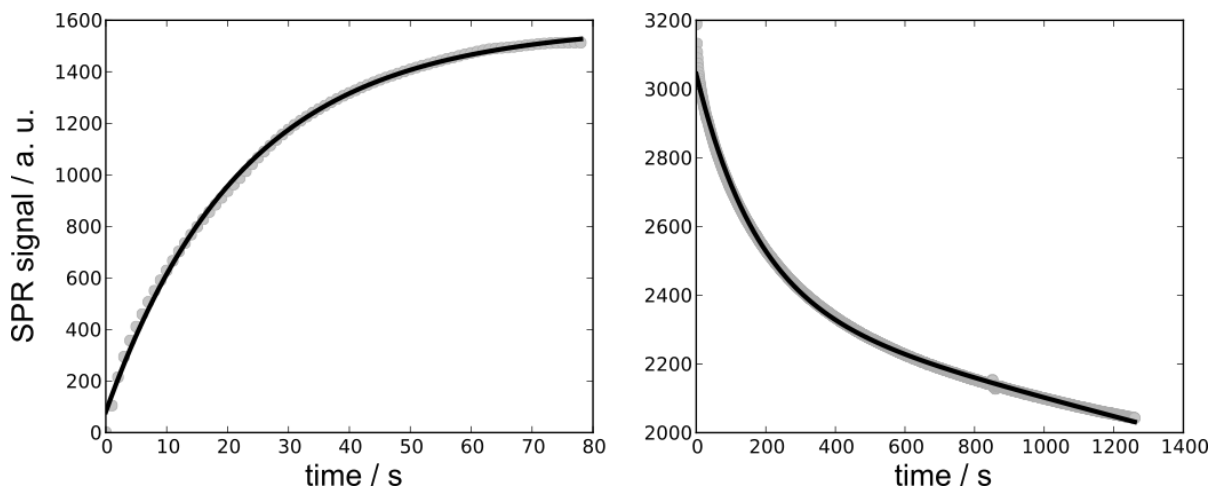
Figure S7: **Fitting of SPR data.** A representative set of fitted SPR data at a monomer concentration of 7 μM for the adsorption part of the experiment (left), at an ionic strength of 32 mM. The adsorption part of the data (left) were fitted to equation S14, the desorption part to equation S13.

2.5 Debye Hückel analysis

Using the Bronsted-Bjerrum equation, which is based on a simple Debye-Hückel model of activity coefficients[6, 2, 1], we obtain at room temperature

$$\log_{10}(k) \approx \log_{10}(k_0) + 0.5z_A z_B \sqrt{I} \tag{S15}$$

where k is the rate at ionic strength I, k_0 is the rate at 0 ionic strength and z_A and z_B are the charges of the reacting species. Therefore the slope of a plot of the logarithm of the rate versus the square root of the ionic strength gives the charges of the reacting species. For the combined rate constants we obtain here, e.g. $k_n k_+$, the slope will be the sum of the products of the charges for each of the two reactions.

3   Seeded experiments and analysis

3.1   Low concentration seeding

In order to confirm that secondary processes do indeed dominate at all salt concentrations, we performed seeded experiments at very low seed concentrations (nM). If the system is dominated by primary nucleation this addition of a very small concentration of seed material has little effect and the half times are expected to remain unchanged. However, if the system is dominated by secondary nucleation these seeds catalyse the formation of more seeds in the positive feedback mechanism of secondary nucleation. This leads to a significant effect on the half times as is apparent at all tested salt concentration, see Fig. S8.
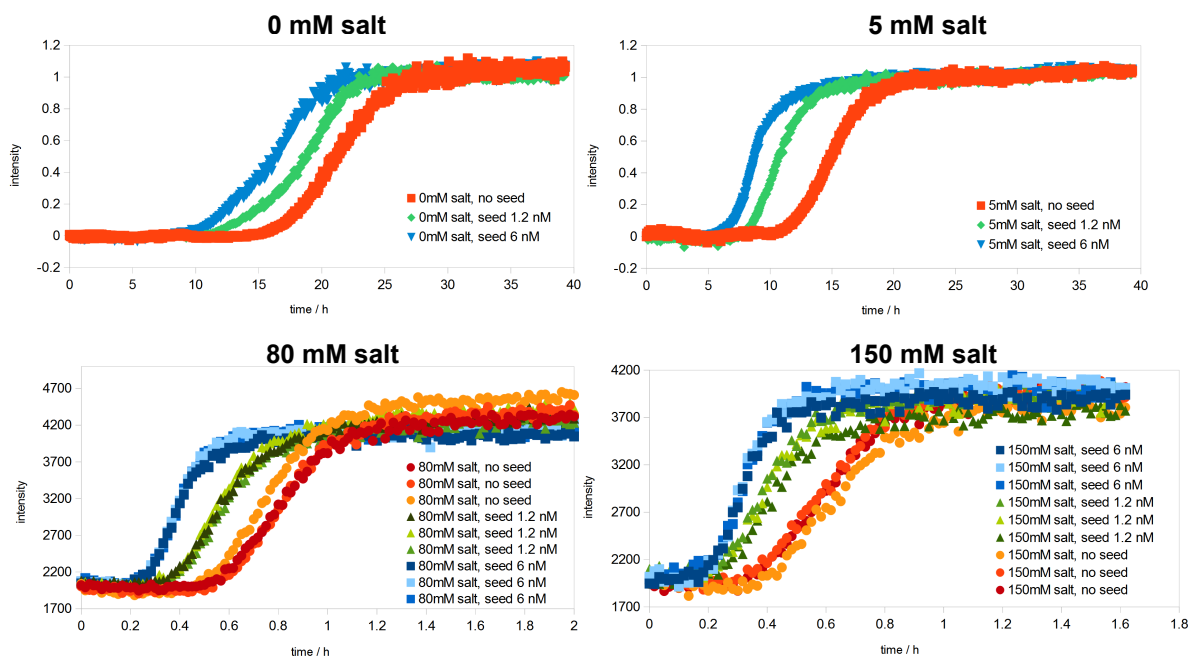

Figure S8: **Effect of low seeding at different salt.** The aggregation of 3 μM Aβ42 at a number of salt concentrations between 0 mM and 150 mM NaCl. The curves at low salt are normalised and averaged over triplicate repeats for reasons of clarity as the variations at these concentrations are large. For the higher salt concentrations the individual curves are shown. In all cases 1.2 nM seeds, corresponding to 0.04% of the monomer concentration present, already lead to a significant shortening of the half time, confirming secondary nucleation is dominant.

3.2 Determination of elongation rate constant

The estimation of the elongation rate also follows the methods described in [9]: Strongly seeded experiments, at a seed concentration of 2 μM and a monomer concentrations ranging from 1 to 6 μM were performed at salt concentrations of 1, 10, 31, 80 ,150, and 300 mM (ionic strengths are 12 mM higher due to the presence of buffer). The initial gradient, $dP/dt|_{t=0} = 2k_+P_0m(t)$, at the different monomer concentrations was used to extract the constant of proportionality, $2k_+P_0$, relating the initial rate to the monomer concentration. This moreover serves as a check for saturation of the elongation rate: If the elongation rate does saturate, then the increase of the initial gradient with monomer concentration is not linear, but plateaus above a certain monomer concentration. No evidence of such a plateau was observed, even at the highest salt concentrations, as evident in Fig. S9. In order to determine the absolute value of the elongation rate
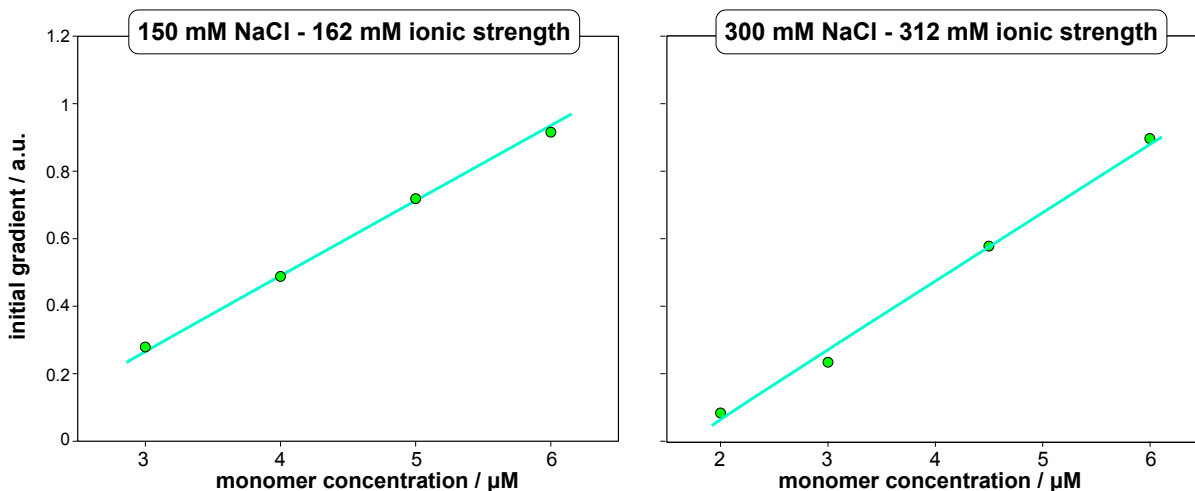

Figure S9: **Initial gradients from strongly seeded experiments.** The initial gradients from strongly seeded experiments (2 μM seeds), show a linear dependence on the monomer concentration, even at high ionic strengths, suggesting that the elongation rate is not yet beginning to saturate. The factor of proportionality relating the initial gradient to the monomer concentration can be used to determine the elongation rate constant.

constant, k_+, from this, P_0 needs to be estimated. The average number of monomers per seed fibril, L_0, relates the initial fibril mass concentration, M_0, to the initial fibril number concentration, P_0, by $P_0 = M_0/L_0$. The fibril mass concentration is known and L_0 can be determined from a measurement of fibril dimensions by TEM. Fig. S10 shows a table of the average dimensions of fibrils at the different salt concentrations. By assuming a density of protein of 1.3 g/ml these dimensions can be used in order to calculate the number of monomers per seed fibril, which is plotted in Fig. S10. The absolute values are likely to be very approximate, due to various biases in the extraction of fibril lengths: larger fibrils are harder to detect, as the likelihood of being able to detect both ends is

smaller. Moreover fibrils can form tangles, which will make the ends less accessible and thereby increase the number of fibrils per growth competent end, L_0. However, if we assume this effects similarly affect all salt concentrations, the observed trend will be more reliable than the absolute values. This equally translates to the trend of the elongation rate constant with increasing salt: although its absolute value is inaccurate due to the errors associated in determining the seed length, its increase by an order of magnitude is significant. The error bars shown in Fig. 6 are hence determined by the inaccuracies in measuring the initial gradient and in extrapolating the seed length to salt concentrations not measured explicitly (Fig. S10).

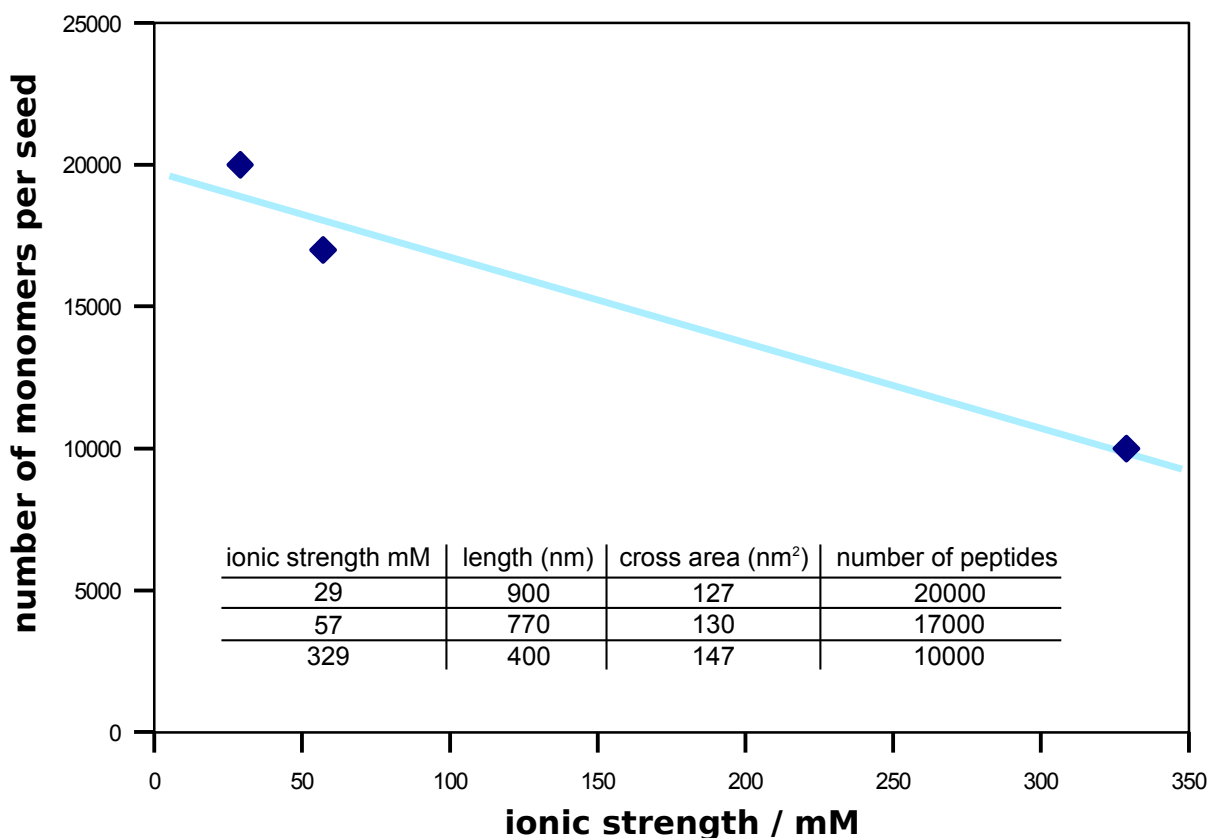| ionic strength mM	length (nm)	cross area (nm²)	number of peptides
29	900	127	20000
57	770	130	17000
329	400	147	10000

Figure S10: **Determination of fibril dimensions from TEM.** A slight decrease in fibril length upon increase in ionic strength can be observed. This trend is in agreement with our finding that the elongation rate increases less than the nucleation rates, leading to a shorter equilibrium fibril length.

4 Further experimental and theoretical techniques

4.1 Protein purification

Initially Aβ42 was isolated from urea-dissolved inclusion bodies via ion exchange, SDS PAGE analysis is shown in Fig. S11. All steps were performed in batch format using a Büchner funnel and a vacuum flask. After application, the resin was washed with 10 mM Tris/HCl, 1 mM EDTA, pH 8.5 (buffer A) with 10 mM NaCl (lane w). The Aβ42 peptide was then eluted with buffer A with 75 mM NaCl. The first five fractions (lanes 1, 2, 3 ,4 and 5) are shown in Fig. S11. The NaCl eluates were passed through 30 kDa Mw cutoff centrifugal filter (Vivaspin, Hydrosart membrane), lyophylized, dissolved in 6M GuHCl, pH 8.5, and separated on a 2.6 x 60 cm Superdex 75 column in 20 mM sodium phosphate, 0.2 mM EDTA, pH 8.5 (buffer B) and lyophylized as multiple identical aliquots. Aliquots were dissolved in 1 mL 6M GuHCl, pH 8.5 and separated on a 1.0 x 30 cm Superdex 75 column in buffer B. The monomer was collected, lyophylized, dissolved in 1 mL 6M GuHCl, pH 8.5, and separated on a 1.0 x 30 cm Superdex 75 column in 20 mM sodium phosphate, 0.2 mM EDTA, pH 8.0. The chromatogram is shown in Fig. S11. The monomer sample used in the kinetic experiments, marked by arrows in Fig. S11, was diluted with water to contain 5-7 μM Aβ42 in 4 mM sodium phosphate, 0.04 mM EDTA, pH 8.0.
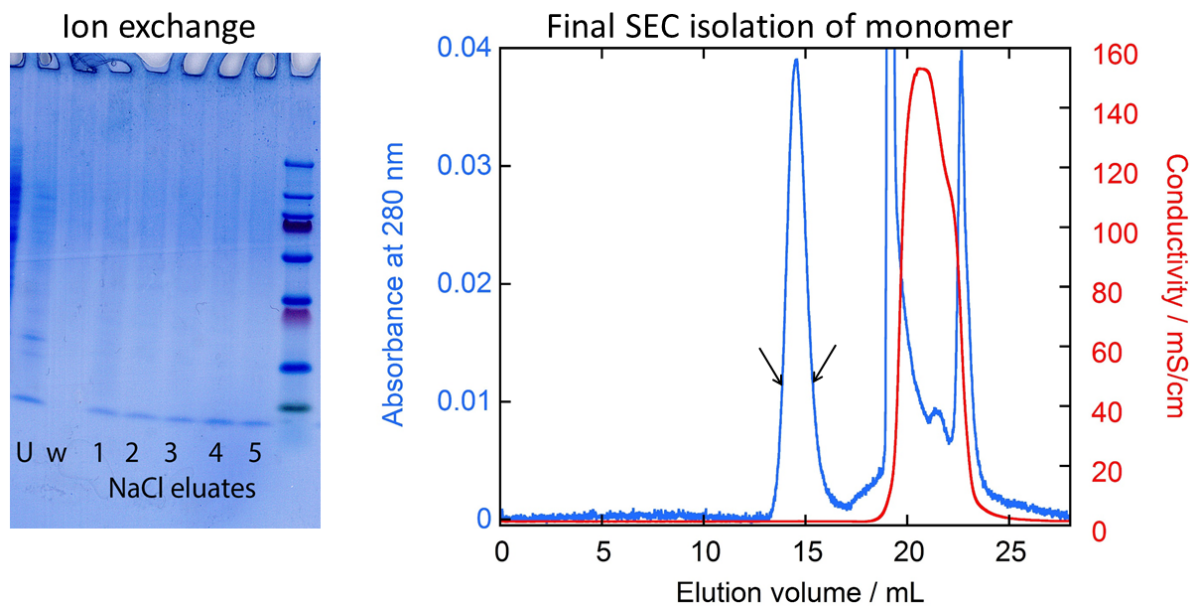
Figure S11: **Examples of data from the isolation and purification of monomeric Aβ42. Left**: SDS PAGE (10-20% Tris-Tricine gel) analysis of the ion exchange step used for the initial isolation of Aβ42 from urea-dissolved inclusion bodies (lane U) using DEAE cellulose anion exchange resin. After application, the resin was washed with 10 mM Tris/HCl, 1 mM EDTA, pH 8.5 (buffer A) with 10 mM NaCl (lane w). The Aβ42 peptide was then eluted with buffer A with 75 mM NaCl. The first five fractions (lanes 1, 2, 3 ,4 and 5) are shown. The last lane contains pre-stained Mw markers. The green protein with highest migration has a Mw of ca. 10 kDa. In lanes U and 1-5, Aβ42 is seen as the band with higher migration than the green marker. **Right**: The monomer was separated on a 1.0 x 30 cm Superdex 75 column in 20 mM sodium phosphate, 0.2 mM EDTA, pH 8.0, the chromatogram (with absorbance in blue and conductivity in red) shows an example of such a third round of gel filtration. The monomer sample used in the kinetic experiments was collected between the arrows.

4.2 Verification of ThT scaling

We have previously optimised the ThT concentrations for measuring Aβ42 aggregation at intermediate ionic strengths[3]. To ensure that the system is still well behaved at higher and lower ionic strengths, i.e. that the fluorescence intensity still scales linearly with the total aggregate concentration, we plotted the plateau fluorescence intensity versus total monomer concentration for a range of ionic strengths. The plots are shown in Fig. S12 and Fig. S13.
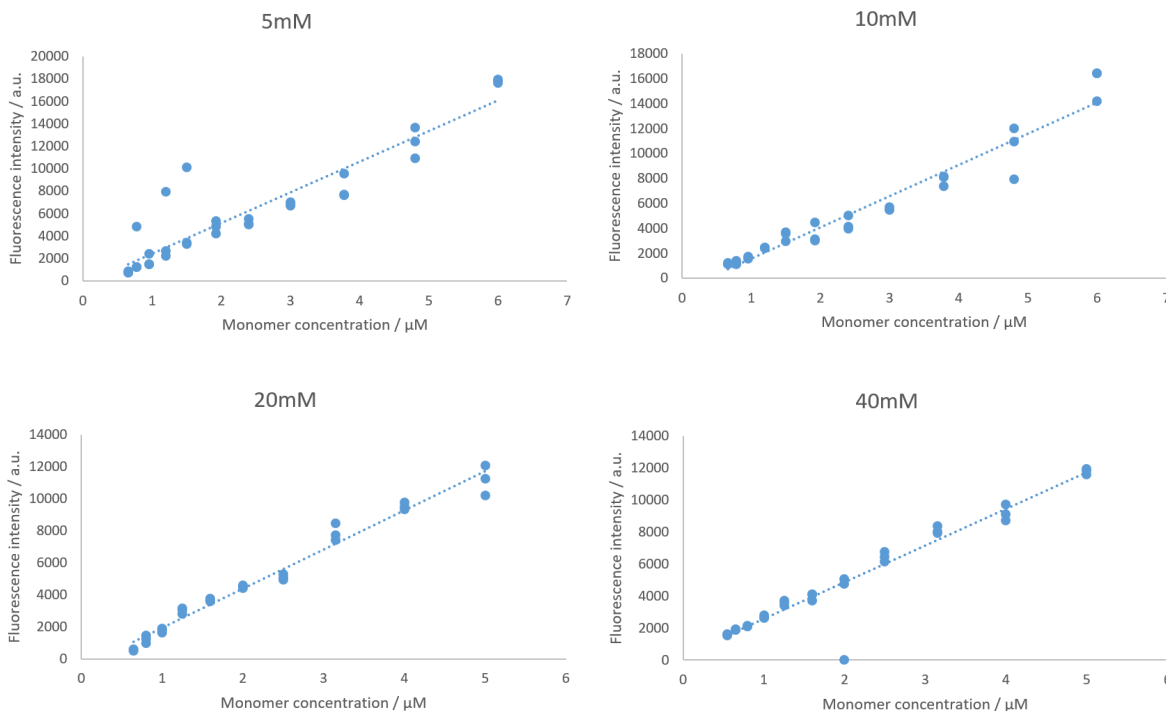

Figure S12: **Scaling of fluorescence with total aggregate mass.** The average fluorescence intensity of the last 25 points in the measurement is plotted against the total monomer concentrations, at NaCl concentrations ranging from 5 mM to 40 mM. The fluorescence intensity scales linearly with the amount of monomer at all salt concentrations.

4.3 Error estimation

The error estimation was based on the method described in [9], similar to a bootstrapping approach: All experiments were performed as triplicate repeats, therefore in order to obtain an estimate of the error in the rate constants due to experimental variations, we considered subsets of the data, including one repeat only at each monomer concentration.
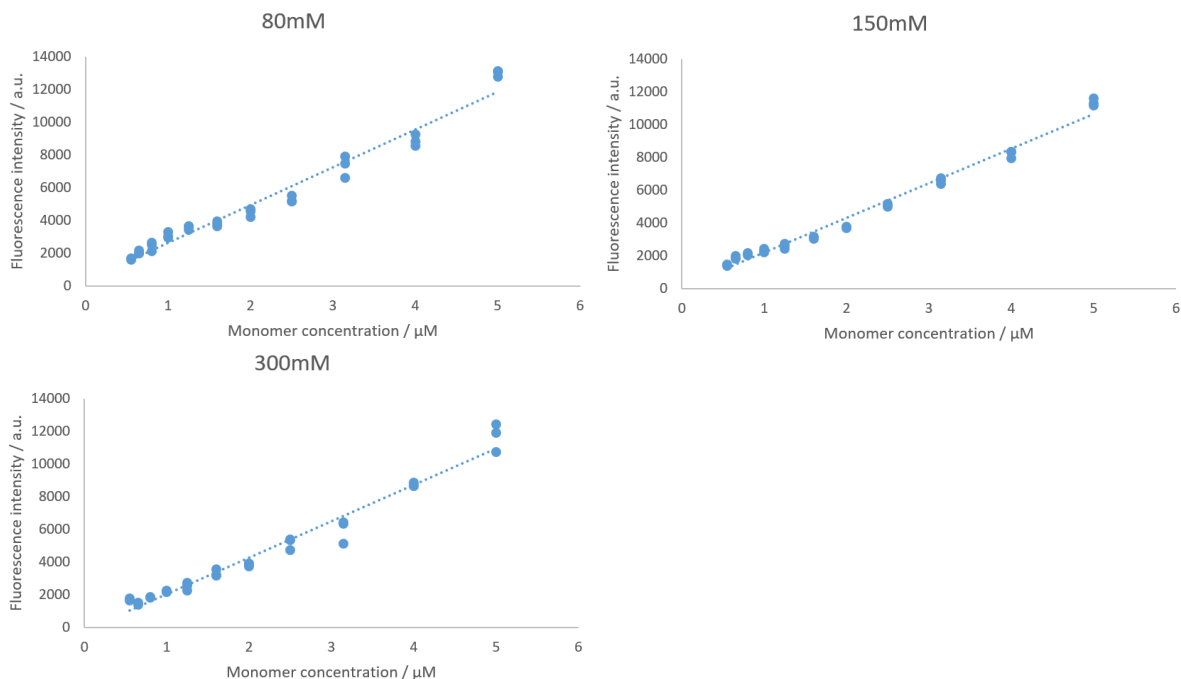
Figure S13: **Scaling of fluorescence with total aggregate mass.** The average fluorescence intensity of the last 25 points in the measurement is plotted against the total monomer concentrations, at NaCl concentrations ranging from 80 mM to 300 mM. The fluorescence intensity scales linearly with the amount of monomer at all salt concentrations.

These subsets were fitted normally and the resulting values of the rate constants were averaged and their standard deviation used to obtain an estimate of the error.

4.4   Fitting algorithm

The fitting was performed using our protein aggregation fitting software, AmyloFit[8], which can be found at www.amylofit.ch.cam.ac.uk. It employs a basin hopping algorithm [10], which consists of a local minimisation paired with a Monte-Carlo step to randomise initial guesses. This algorithm thereby effectively flattens the potential energy landscape and allows the fit to converge to the global minimum even if the initial guess was not in the correct basin of attraction. Such a property is important in the global fitting of large datasets to complex equations as these situations tend to result in rough energy landscapes and convergence to local rather than the global minimum can be an issue.

References

[1] Niels Bjerrum. Zur theorie der chemischen reaktionsgeschwindigkeit. *Z. Physik. Chem.*, 108:82, 1924.

[2] J. N. Bronsted and C. E. Teeter. On kinetic salt effect. *The Journal of Physical Chemistry*, 28(6):579–587, 1923.

[3] Samuel I. A. Cohen, Sara Linse, Leila M. Luheshi, Erik Hellstrand, Duncan A. White, Luke Rajah, Daniel E. Otzen, Michele Vendruscolo, Christopher M. Dobson, and Tuomas P. J. Knowles. Proliferation of amyloid-beta42 aggregates occurs through a secondary nucleation mechanism. *Proceedings of the National Academy of Sciences*, 110:9758–9763, 2013.

[4] Samuel I A Cohen, Michele Vendruscolo, Christopher M Dobson, and Tuomas P J Knowles. Nucleated polymerization with secondary pathways. ii. determination of self-consistent solutions to growth processes described by non-linear master equations. *J Chem Phys*, 135(6):065106, 2011.

[5] Samuel I A Cohen, Michele Vendruscolo, Mark E Welland, Christopher M Dobson, Eugene M Terentjev, and Tuomas P J Knowles. Nucleated polymerization with secondary pathways. i. time evolution of the principal moments. *J Chem Phys*, 135(6):065105, 2011.

[6] P Debye and E Hückel. Zur theorie der elektrolyte. i. gefrierpunktserniedrigung und verwandte erscheinungen. *Phys. Z*, 24:185, 1923.

[7] Gonzalo A. Garcia, Samuel I. A. Cohen, Christopher M. Dobson, and Tuomas P. J. Knowles. Nucleation-conversion-polymerization reactions of biological macromolecules with prenucleation clusters. *Phys. Rev. E*, 89:032712, Mar 2014.

[8] Georg Meisl, Julius B. Kirkegaard, Paolo Arosio, Thomas T. C. Michaels, Michele Vendruscolo, Christopher M. Dobson, Sara Linse, and Tuomas P. J. Knowles. Molecular mechanisms of protein aggregation from global fitting of kinetic models. *Nature Protocols*, 11(2):252–272, 2016.

[9] Georg Meisl, Xiaoting Yang, Erik Hellstrand, Birgitta Frohm, Julius B. Kirkegaard, Samuel I. A. Cohen, Christopher M. Dobson, Sara Linse, and Tuomas P. J. Knowles. Differences in nucleation behavior underlie the contrasting aggregation kinetics of the aβ40 and aβ42 peptides. *Proceedings of the National Academy of Sciences*, 111:9384–9389, 2014.

[10] David J. Wales and Jonathan P. K. Doye. Global optimization by basin-hopping and the lowest energy structures of lennard-jones clusters containing up to 110 atoms. *The Journal of Physical Chemistry A*, 101(28):5111–5116, 1997.